Eur. Phys. J. Special Topics **165**, 151–160 (2008)

DOI: 10.1140/epjst/e2008-00858-8

THE EUROPEAN PHYSICAL JOURNAL SPECIAL TOPICS

An analysis of a two cylinder-fluid interaction at critical gap spacing by a cell boundary element method

A.B. Ravi[1,a], M. Tan[2], and W.G. Price[2]

[1] University of Aberdeen, Dept. of Geology and Petroleum geology, Kings College, Aberdeen AB24 3UE, UK
[2] School of Engineering Sciences, Ship Science, University of Southampton, Highfield, Southampton SO17 1BJ, UK

Abstract. Incompressible viscous, uniform flow past two parallel cylinders of equal diameter at a critical gap spacing $g^* = 0.90$ to 1.10 is investigated using the viscous cell boundary element method. In this critical flow zone an irregular interchange of in-phase and anti-phase wake flows is observed and the switching mechanism between the states is investigated. Numerical studies undertaken at space increments of 0.05, including the central case $g^* = 1.0$, detail the flow characteristics in time and space domains. Probability and power spectral analyses are presented to illustrate the statistical characteristics of the drag and lift flow parameters and vortex shedding patterns assessed through examination of their frequencies.

1 Introduction

Viscous fluid flows around cylinders exhibit a plethora of fluid mechanics phenomenon including flow separation, vortex shedding, turbulence, etc. They are of significance in predicting the loads on structures subject to fluid motions as discussed by Hatton (1999) for the design of deepwater floating oil production systems involving risers, tension leg platforms, fixed jacket structures, etc. For such configurations a two-dimensional analysis is considered sufficient for the evaluation of the forces acting on these offshore structures since the vertical component of velocity is neglected as discussed by Zhou & Graham (2000). The fluid-structure interactions occurring have similarity to studies of a planar flow around cylinders subject to sinusoidal loading and they are of importance to vortex-induced vibration fatigue damage.

Vortex interactions with foils, blades or cylinders can result in significant changes in the velocity field, vortex shedding from the body surface and damage to the structure. For example, vortex shedding and interaction cause distortion to the local heat transfer mechanism as in the case of turbine blades. Rockwell (1998) reviewed the challenging problems arising from the interaction of vortices in three-dimensional flow and the resultant local loading.

The flow parameters important to the vortex shedding are the Reynolds number defined as $R_e = UD/\nu$ and the Strouhal number defined as $S = fD/U$ where U, D, ν and f are the free stream velocity, cylinder diameter, kinematical viscosity of the fluid and the vortex shedding frequency, respectively. Direct Numerical Simulation (DNS) of the Navier-Stokes equations, to analyse the vortex dynamics of fluid-structure interaction, is limited to moderately low Reynolds number ($R_e < 10000$) unless sub-grid scale turbulence models are used as discussed by Cheng & Armfield (1994). This technique complements previous approaches to examine vortex shedding and wakes by Mair & Maull (1971), Bearman & Graham (1980), Oertel (1990), to name but

[a] e-mail: ravi@abdn.ac.uk

a few. Effective wake control is possible due to the existence of absolutely unstable regions at super-critical Reynolds number providing explanation of physical interaction phenomenon and to the reformulation of von Karman stability theory of vortex streets in near and far fields.

For side-by-side cylinder arrangements, the vortex formation in the forced system of flow exhibits cross-coupling between the wakes evolved from the neighbouring cylinders and their interaction. Such mechanisms cause alteration to the pressure distribution in the fluid domain, a predominant vortex frequency value and forces acting on the cylinders. The investigations of Mahir & Rockwell (1996) show that the lock-on response frequency range is of the same order as occurs for an equivalent single cylinder with a shift to higher frequencies and to lower amplitudes. The experimental studies of Williamson (1985) clearly illustrate the formation of two parallel vortex streets. When shedding is in anti-phase, two distinct vortex streets are visible and when shedding occurs in-phase, a single *binary vortex* large scale wake is formed created by the superposition of neighbouring wakes. Even though the flow exhibits many anomalies and distortions in the transitional or turbulent flow regime, the evidence presented shows a close analogy to the observed flow in the lower Reynolds number flow regime in its macroscopic characteristics. This has encouraged many numerical studies in the low Reynolds number flow regime see, for example, Persillon, Braza & Jin (1995), Zhang & Zhang (1997), to name but a few.

Ng & Ko (1995) concluded that the flow around equal diameter cylinders placed side by side, with a non-dimensional separation gap $g^* = 0.75$ to 1.25 which is defined as the ratio of the clearance distance between the cylinders to the cylinder diameter, exhibits chaotic and bistable characteristics through a little understood irregular switching mechanism. The novelty of the present numerical study is, therefore, to reveal the details of the flow characteristics in this critical zone together with statistical measures in both time and space. Investigations are performed for gap width $g^* = 0.90$ to 1.10 in increments of 0.05 and it is found that although the flows exhibit irregular behaviour a process with strong periodic components is observed.

2 Mathematical model

Price & Tan (1992a, b), Tan (1994), Tan, Farrant & Price (1999) developed a cell viscous boundary element method to solve Navier-Stokes fluid flow problems. This has proved very successful in solving fluid-structure interaction problems involving multi-body configuration as discussed by Farrant (1998), Farrant, Tan & Price (2000, 2001) and Uzunoglu, Tan & Price (2001).For these reasons, details of the numerical approach are omitted and only a brief description of the method is included herein. The numerical scheme of study is a hybrid approach combining boundary element and finite element methods. The boundary element is applied to fluid cells idealising the fluid domain through an unstructured mesh and global equations are obtained by finite element procedures.

Figure 1 illustrates a discretised fluid domain adopting an unstructured mesh involving a number of cell elements.

A typical cell Ω is shown bounded by surface Σ with outward normal $\boldsymbol{n}$. The fluid is assumed incompressible and the governing equations of the flow in terms of a non-dimensional velocity field v_k and the pressure p are given by

$$\dot{v}_j + (v_j v_k)_{,k} + p_{,j} - [\nu_e(v_{j,k} + v_{k,j})]_{,k} = 0, \tag{1}$$

$$v_{j,j} = 0. \tag{2}$$

where $\nu_e (= 1/R_e)$ represents the inverse of the Reynolds number. The subscript index $j = 1, 2$ and $j = 1, 2, 3$ denotes two-dimensional and three-dimensional body-fluid interaction problems respectively.

An integral equation can be formulated from these equations following the methodology of the boundary element method proposed by Tan et al. (1999) who showed that the relevant cell integral equation for incompressible fluid flow may be written in the form,

$$C(\boldsymbol{\xi})v_s(\boldsymbol{\xi}, t) + \sum_{l=1}^{4} v_j^{(l)} \int_{(l)} (\boldsymbol{u} \cdot \boldsymbol{n} v_{sj}^* + R_{sj}^*) d\Sigma = \sum_{l=1}^{4} R_j^{(l)} \int_{(l)} v_{sj}^* d\Sigma + \int_{\Omega} h_j v_{sj}^* \, d\Sigma. \tag{3}$$

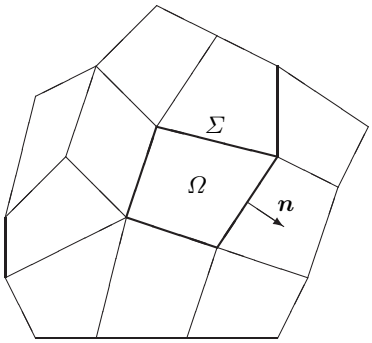

Fig. 1. Discretisation of the fluid domain by an unstructured mesh involving a typical cell Ω bounded by surface Σ with outward normal $\boldsymbol{n}$.

Here $C(\boldsymbol{\xi})$ is a constant of value 0, 0.5 or 1 depending on the location of the fluid point $\boldsymbol{\xi}$ and $\mathbf{u}$ is an averaged value of the velocity on the cell. The weighting functions v^*_{sj} and p^*_s denote fundamental solutions and the function,

$$R^*_{sj} = p^*_s n_j + \nu_e(v^*_{sj,k} + v^*_{sk,j})n_k, \tag{4}$$

R^*_j represents the traction force on the cell boundary and h_j is the resultant term derived from the acceleration $\dot{v}_j$ after a second order time marching procedure is introduced into the finite difference scheme to resolve the non-linear convective term in equation (1). Such a scheme has been shown to be beneficial both analytically and for enhanced computational efficiency.

The application of equation (3) to each cell in the idealised fluid domain generates a set of algebraic equations describing the fluid dynamics in the cell. That is, if the superscript e denotes the *eth* cell, the *eth* algebraic equation is expressed in the form

$$A^{(e)}_{\mathrm{v}} V^{(e)} = A^{(e)}_{\mathrm{r}} R^{(e)} + b^{(e)}. \tag{5}$$

Here,

$$V^{(e)} = \begin{Bmatrix} \boldsymbol{v}^{(1)} \\ \boldsymbol{v}^{(2)} \\ \boldsymbol{v}^{(3)} \\ \boldsymbol{v}^{(4)} \end{Bmatrix}, \qquad R^{(e)} = \begin{Bmatrix} \boldsymbol{R}^{(1)} \\ \boldsymbol{R}^{(2)} \\ \boldsymbol{R}^{(3)} \\ \boldsymbol{R}^{(4)} \end{Bmatrix},$$

are single column arrays constructed from the velocity $\boldsymbol{v}^{(l)}$ and traction $\boldsymbol{R}^{(l)}$ values at the centre of each edge ($l = 1, 2, 3, 4$) of the cell as shown in Figure 2. Tan et al. (1999) define the coefficients

$$A^{(e)}_v = \left[\frac{1}{2}\delta_{sj} + \int_{(l)} (\boldsymbol{u}\cdot\boldsymbol{n} v^*_{sj} + R^*_{sj}) d\Sigma + \frac{3}{8\Delta t}\int_\Omega v^*_{sj} d\Omega\right], \tag{6}$$

$$A^{(e)}_r = \left[\int_{(l)} v^*_{sj} d\Sigma\right], \qquad b^{(e)} = \left\{\frac{(4\bar{v}^{(n)}_j - \bar{v}^{(n-1)}_j)}{2\Delta t}\int_\Omega v^*_{sj}\, d\Omega\right\}. \tag{7}$$

Their forms relate to the second order time marching procedure chosen, and the evaluations of the respective integrals involve the velocity and boundary integrals containing the values of the surface traction force at the collocation points. The single column array $b^{(e)}$ contains entries evaluated from the domain integral incorporating the contribution of the velocity from the last time step $v^{(n)}_j$ averaged across the cell i.e. $\bar{v}^{(n)}_j$. The application of continuity conditions to fluid velocity and surface traction forces at cell interfaces allows a global system of algebraic equations to be derived in the form of

$$DV = F \tag{8}$$

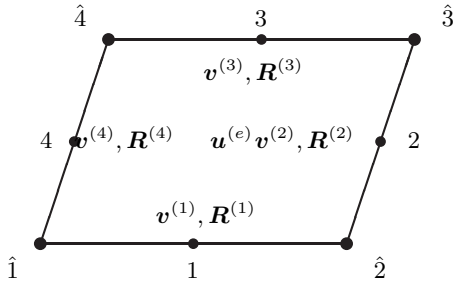

Fig. 2. A typical quadrilateral cell with ordered notation.

where V is the array of velocity values on the collocation points in the assigned global order, D is constructed from combinations of the coefficients $A_{\mathrm{v}}^{(e)}$ and $A_{\mathrm{r}}^{(e)}$ and F represents the contributions from $b^{(e)}$ arising from the global assembly.

The specification of boundary conditions on the global domain, i.e. either velocity V or traction force R, allows solution of the fluid problem as demonstrated by Tan et al. (1999). This cell viscous boundary element method features a high degree of dependence on analytical solutions (i.e. fundamental solutions v_{sj}^{*}, R_{sj}^{*} and integrations) in the mathematical model, allowing retention of accuracy of the solution within the numerical scheme of study. It incorporates a primitive-variable formulation and applies to both structured and unstructured meshes. Furthermore the use of velocity and surface traction force as the basic unknowns provides a convenient way of expressing boundary conditions. The computational domain and the boundary conditions are as shown in Figure 3.

An extensive and detailed numerical validation of the method was undertaken by Farrant (1998) and Farrant et al. (2000, 2001) for various arrangement of cylinders i.e. single, multiple cylinders in tandem, side-by-side, staggered, combination of circular and elliptical cylinders, etc. The influence of mesh refinement, various boundary conditions and domain sizes, time stepping intervals, etc. in the numerical scheme of study were previously investigated through comparisons of predicted values of Strouhal number, lift coefficient, drag coefficient, flow field pattern, etc. against other predictions using different theoretical approaches and against the experimental evidence provided by Williamson (1985). Such studies are not reproduced here but their findings are incorporated into the present investigation involving a flow of Reynolds number $R_e = 100$, a second order time stepping procedure using time step interval $t = 0.02$ which was shown previously to ensure convergence of solution.

3 Numerical predictions

3.1 Time simulations

Adopting the flow doping procedure described by Tan et al. (1999), Figure 4 illustrates the vortex wake patterns developed behind the cylinder for gap separations $g^* = 0.95$, 1.0 and 1.05 respectively. These records extend approximately 50 cylinder diameters downstream producing a simulation length of 2500 time steps. If required, these records may be extended but the lengths presented illustrate typical patterns. Farrant et al. (2000) previously showed that the wake developed behind side-by-side cylinders at different spacing simulates closely the experimental evidence observed by Williamson (1985).

These wakes show distinctively different patterns resulting from the shedding and interaction between the shed vortices. Namely there is a tendency for in-phase vortex shedding at $g^* = 0.95$ and for anti-phase vortex shedding at $g^* = 1.05$ as described by Farrant et al. (2001). The former pattern indicates strong mixing and the wake generated is more spread and diffuse whereas, the latter shows less mixing with the vortices merging to create a tighter spatial wake. During simulations it was noted that switching of in-phase and anti-phase shedding with time was possible in both cases. In some senses, the pattern displayed for $g^* = 1.0$ exhibits a transition

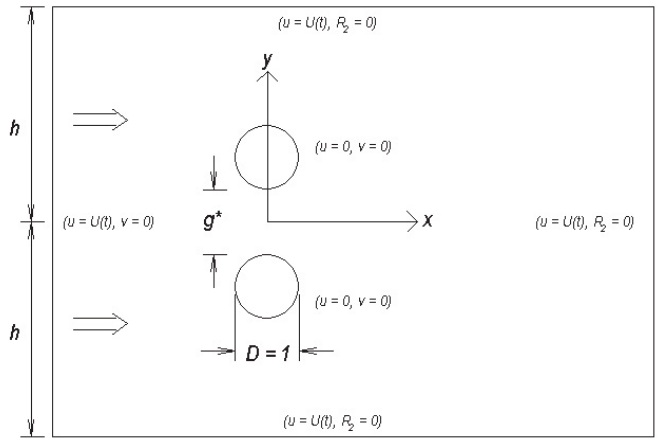

Fig. 3. Computational domain definition and boundary conditions for cylinders in uniform flow.

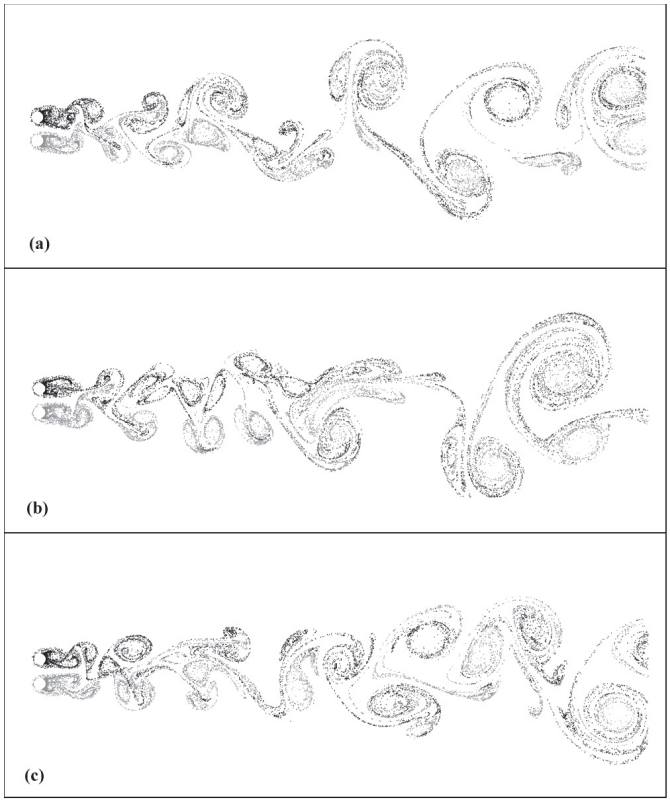

Fig. 4. Wake patterns generated behind side-by-side cylinder of equal diameter for (a) $g^* = 0.95$ (b) $g^* = 1.00$ (c) $g^* = 1.05$.

phase where thorough mixing and vortex merging occurs. At this separation switching between phases is more likely to arise and a less structured wake pattern is observed but there remains an underlying structure to the flow as indicated by statistical data.

Figure 5 illustrates the typical time records of predicted lift coefficient, C_l, and drag coefficient, C_d, experienced by the *lower cylinder* for gap separation $g^* = 1.0$. Here the drag and lift coefficients are calculated using drag and lift forces divided by $1/2\rho U^2 D$, where ρ, U and D are fluid density, free stream velocity and cylinder diameter. These records extend to over 2000 time step intervals and display distinct patterns. The lift coefficient record clearly shows a beat

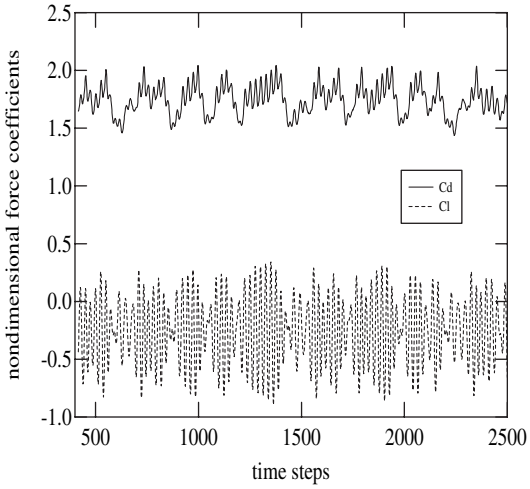

Fig. 5. Superposition of C_l and C_d records with time illustrating the different characteristics for $g^* = 1.00$.

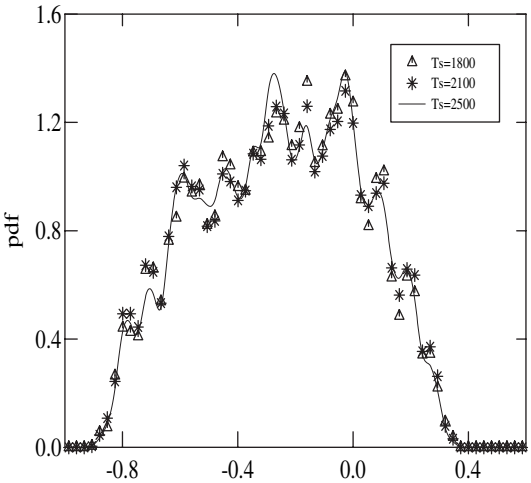

Fig. 6. Variation of probability density function for lift C_l at $g^* = 1.00$ for different intervals of simulated record length $T_s = 1800, 2100, 2500$ step intervals.

characteristic about a mean value $C_l = -0.26$. The negative sign signifies a repulsive force. The drag coefficient signal shows less amplitude variation but a more spiky pattern about a mean value $C_d = 1.74$. Figure 5 shows a comparison of both signals reflecting the marked differences in these record characteristics. In this investigation, wake vortex patterns were generated for a wide range of different simulation lengths and the selected data presented are typical of the extensive data base created.

3.2 Statistical measures

From the presented time records, statistical measures (i.e mean values, probability density functions, spectral densities, etc.) were deduced to provide insights into the mechanisms and behaviour characteristics occurring in the observed complex fluid-structure interaction.

Figure 6 and Figure 7 illustrate the variation of the probability density functions for lift and drag respectively with different simulated record lengths for $g^* = 1.0$. In each case slight

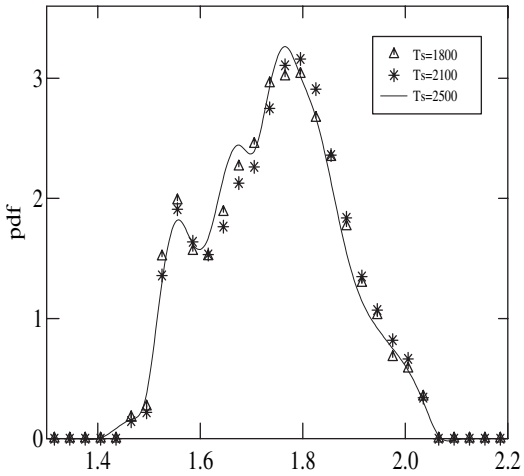

Fig. 7. Variation of probability density function for drag C_d at $g^* = 1.00$ for different intervals of simulated record length $T_s = 1800, 2100, 2500$ step intervals.

Table 1. Comparison of Strouhal number (S), drag (C_d) and lift (C_l) flow parameters for different gaps between cylinders (g^*) and lengths of simulation time step intervals (T_s).

g^*	T_s	C_{dmean}	C_{lmean}	C_{dmax}	C_{lmax}	S
	1800	1.73	−0.28	2.08	0.24	
0.90	2100	1.73	−0.29	2.08	0.24	0.195
	2500	1.73	−0.29	2.08	0.24	
	1800	1.73	−0.27	2.09	0.26	
0.95	2100	1.73	−0.27	2.09	0.26	0.215
	2500	1.73	−0.27	2.09	0.26	
	1800	1.75	−0.26	2.04	0.34	
1.00	2100	1.75	−0.26	2.04	0.34	0.195
	2500	1.74	−0.26	2.04	0.34	
	1800	1.74	−0.25	2.04	0.34	
1.05	2100	1.74	−0.25	2.04	0.34	0.176
	2500	1.73	−0.26	2.04	0.34	
	1800	1.74	−0.24	2.03	0.38	
1.10	2100	1.73	−0.24	2.03	0.38	0.176
	2500	1.73	−0.24	2.03	0.38	

variations between curves are observed for the chosen record length but each set of data demonstrates the same distinctive trends. In subsequent analyses, the 2500 step interval records are used for comparison purposes.

Table 1 shows data derived from the various time records T_s at each separation gap g^* and their sensitivity to these control variables. The mean drag coefficient values indicate little variation with g^* and T_s displaying a very slightly increased value at $g^* = 1.0$. The mean lift coefficient values demonstrate more variation with different gap size and simulation length. It is observed that a maximum value occurs at $g^* = 0.90$ which decreases as g^* increases in value. At each gap size and varying T_s value the maximum drag coefficient C_{dmax} and lift coefficient C_{lmax} remain constant displaying invariance to T_s value. Variation in these parameters is observed with changing value of g^* with C_{dmax} showing a decreasing trend from the range

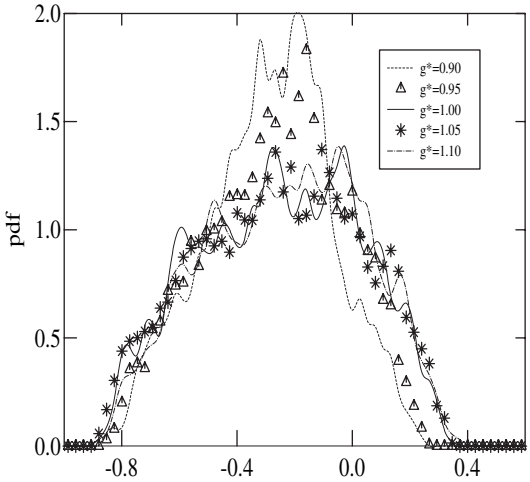

Fig. 8. Variation of probability density function for lift C_l for simulated record length of 2500 step intervals for separation gap $g^* = 0.90, 0.95, 1.00, 1.05, 1.10$.

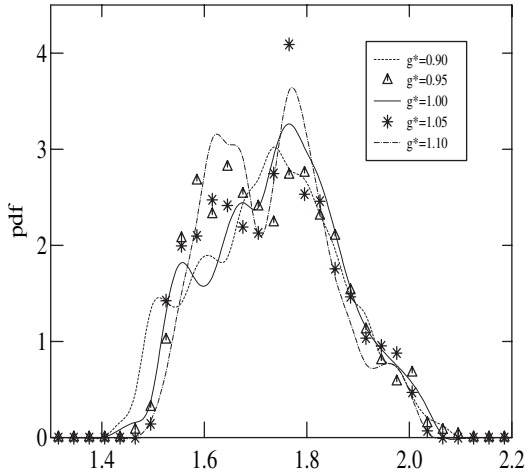

Fig. 9. Variation of probability density function for drag C_d for simulated record length of 2500 step intervals for separation gap $g^* = 0.90, 0.95, 1.00, 1.05, 1.10$.

$0.90 \leq g^* \leq 0.95$ and C_{lmax} displaying an increasing trend as g^* value increases. The largest variation in this data set is illustrated in the changing value of Strouhal number with g^* which reaches a maximum value at $g^* = 0.95$.

Figure 8 and Figure 9 display the variation of the probability density functions for lift and drag respectively for different gap separation g^*. Although the maximum values of the probability density functions for lift show variation the overall shape of the five curves demonstrates similarity. Figure 8 shows that as the separation gap increases from $g^* = 0.90$ the more pronounced probability density function peak feature observed at $g^* = 0.90$ decreases to a relatively flat parabolic curve at $g^* = 1.10$. The features displayed in Figure 9 for the drag probability density function show a measure of similarity with a more pronounced peak structure at $g^* = 0.95$, 1.05 and 1.0.

Typical lift and drag power spectra curves are displayed in Figure 10 and Figure 11 for $g^* = 0.90$. The lift coefficient spectral density with its dominant low frequency content displays a maximum value at the Strouhal frequency. The lower frequency peak observed in the power spectra curves is of value comparable to the envelope frequency of the C_l curve illustrated in Figure 5. A similar pattern is observed in the drag coefficient spectral density curve but in the

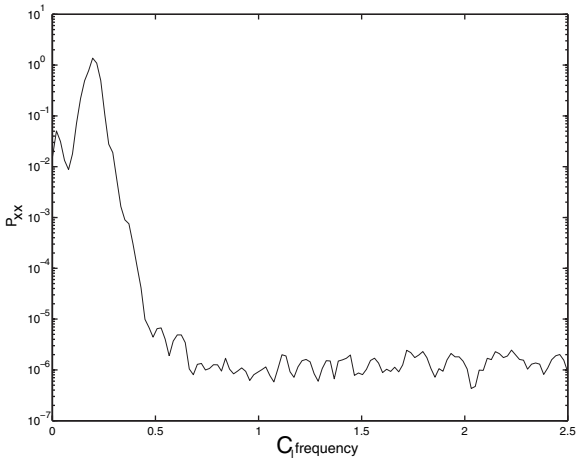

Fig. 10. Typical variation of power spectral density for lift coefficients C_l.

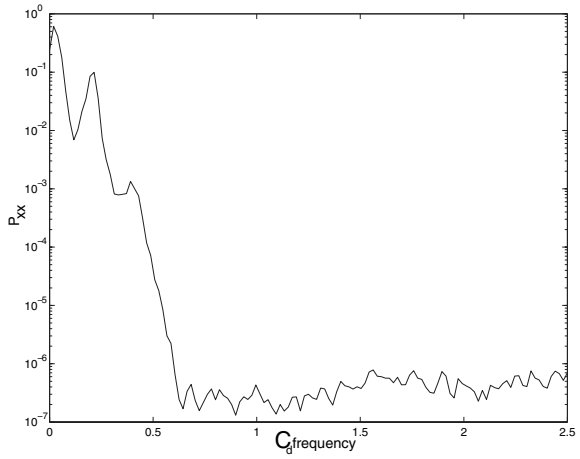

Fig. 11. Typical variation of power spectral density for drag coefficients C_d.

low frequency region, three shedding frequencies are seen with the Strouhal frequency, not displaying a similar dominance as in the lift coefficient case. As seen, the third peak is insignificant compared with the other two.

4 Conclusion

For parallel cylinders, with spacing $g^* = 0.95$ to 1.05, placed in a uniform viscous flow ($R_e = 100$) the predicted vortex patterns show dependence on the spacing factor which also relates to the interaction mechanism and vortex shedding frequency. Namely, for $g^* = 0.95$ an in-phase vortex shedding pattern occurs with strong vortex mixing, a diffused wake and a maximum Strouhal frequency value. In contrast at $g^* = 1.05$ an anti-phase vortex pattern dominates with weak vortex mixing, a tighter spatial wake and the Strouhal frequency tends to a minimum value. At the critical value of $g^* = 1.0$, a thorough mixing and amalgamation of vortex occurs with an intermediate Strouhal frequency value. The in-phase and anti-phase vortex shedding switching is observed and a less structured wake occurs. Although this behaviour is irregular, the statistical measures reveal strong periodic components in the data sets. Further studies are needed, however, to identify clearly the existence of chaotic behaviour of the system based on the studies of Lyapunov exponents, or entropies.

It is also observed that for $g^* < 1.0$, the vortex wake is influenced by in-phase vortex shedding whereas for $g^* > 1.0$ anti-phase vortex shedding is more evident.

References

1. P.W. Bearman, J.M.R. Graham, J. Fluid Mech. **99**, 225 (1980)
2. L. Cheng, S.W. Armfield, Proc. Boss **94**, 655 (1994)
3. T. Farrant, *The Boundary Element Method Applied to Viscous and Vortex Shedding Flows around Cylinders* (Ph.D Thesis, University of Southampton, Southampton, UK, 1998)
4. T. Farrant, M. Tan, W.G. Price, J. Fluids Struct. **14**, 375 (2000)
5. T. Farrant, M. Tan, W.G. Price, Comput. Fluids **30**, 211 (2001)
6. S.A. Hatton, *Society of Underwater Technology* (University of Newcastle, UK, 1999)
7. N. Mahir, D. Rockwell, J. Fluids Struct. **10**, 491 (1996)
8. W.A. Mair, D.J. Maull, J. Fluid Mech. **45**, 209 (1971)
9. C.W. Ng, N.W.M. Ko, J. Wind, Eng. Industr. Aerodyn. **54/55**, 277 (1995)
10. J.H. Ortel, Ann. Rev. Fluid Mech. **22**, 539 (1990)
11. H. Persillon, M. Braza, G. Jin, *Proceedings of 5th International Offshore and Polar Engineering Conference* (International Society of Offshore and Polar Engineers, 1995), p. 597
12. W.G. Price, M. Tan, *Proceedings of Royal Society London,* 1992 (A438), pp. 447
13. W.G. Price, M. Tan, *Proceedings of international conference on the Dynamics of Marine Vehicles and Structures in Waves* (1990), p. 125
14. D. Rockwell, Ann. Rev. Fluid Mech. **30**, 199 (1998)
15. M. Tan, *A Viscous Boundary Element Method Approach to Fluid Flow-Structure Interaction Problems*, Ph.D. thesis (University of Southampton, Southampton, UK)
16. M. Tan, T. Farrant, W.G. Price, Proc. Royal Soc. London A **455**, 4277 (1999)
17. B. Uzunoglu, M. Tan, W.G. Price, Int. J. Numer. Meth. Eng. **50**, 2317 (2001)
18. C.H.K. Williamson, J. Fluid Mech. **155**, 141 (1985)
19. H. Zhang, X. Zhang, Comput. Fluids **26**, 83 (1997)
20. C.Y. Zhou, J.M.R. Graham, J. Fluids Struct. **14**, 403 (2000)